Nano-Patterned Wetting Layers on Silicone Hydrogels: Toward Continuous-Wear Contact Lenses with Enhanced Oxygen Flux

Labishetty Sai Charan[1]*, Navjyot S Trivedi[2], Tara Rani[1], Logesh Babu[1]

[1]Department of Optometry, University Institute of Allied Health Sciences, Chandigarh University, Punjab, India
[2]Department of Physiotherapy, University Institute of Allied Health Sciences, Chandigarh University, Punjab, India

Charansai184@gmail.com

Abstract.
Silicone-hydrogel (SiHy) lenses solved corneal hypoxia two decades ago, yet their hydrophobic skins still invite lipid gunk, bacterial hitch-hikers and end-of-day burn. Nano-patterned wetting layers (NPWLs)—comprising sub-500 nm grooves, pillars, and honeycomb pores—were fabricated via embossing or self-assembly in a single post-moulding step. NPWLs were fabricated via UV-imprint/self-assembly, with modulus parity (nanoindentation) and debris safety (STEM/macrophage assays). By pinning a nanoscopic water sheet to the lens front, these textures slash contact-angle hysteresis below 4°, treble tear-film break-up time, and lift functional oxygen transmissibility past the 150 Barrer cm^{-1} mark without stealing a molecule of polydimethylsiloxane (PDMS) from the bulk. Quantitative assays confirm the promise: protein-lipid deposition drops 60–70 %, Pseudomonas and Staphylococcus adhesion fall an order of magnitude, and ex-vivo corneas swell a mere 3.5 % after an overnight run. In the first 30-night human crossover, wearers logged an 11-point comfort jump on a 100-point scale and halved dropout rates versus best-in-class SiHy controls.

Manufacturing economics are equally persuasive. Volatile organic compound -free Ultra violet (UV)-imprint resins and water-borne layer-by-layer coatings add ≤ United States Dollar 0.03 per lens at one-million-unit monthly throughput while trimming the carbon footprint by 0.9 kg CO_2-eq per million pieces. Mechanical-modulus parity and a negligible nano-debris profile position NPWL lenses for Food and Drug Administration Special 510(k) clearance and European Union Medical Device Regulation class IIb listing. Beyond comfort and oxygen, the patterned scaffolds offer plug-and-play docking sites for antimicrobial peptides or mechano-responsive drug depots, opening a roadmap toward truly therapeutic, week-long lenses.

S. Kumar et al. (eds.), *Proceedings of the 2nd International Conference on Advanced Materials & Devices for Futuristic Applications-2024 (IC-AMDFA 2024)*, Atlantis Highlights in Materials Science and Technology 5,
https://doi.org/10.2991/978-94-6239-695-1_4

Keywords: Nano-patterned wetting layer; Silicone-hydrogel lenses; Oxygen transmissibility; Tear-film stability; Biofouling mitigation; Sustainable manufacturing

1 Introduction & Scope

1.1 Historical Perspective of Silicone-Hydrogel Contact Lenses

Commercialization of silicone-hydrogel (SiHy) lenses at the turn of the century addressed the chronic hypoxia that plagued first-generation hydrogel materials by embedding poly(dimethyl-siloxane) segments that support oxygen permeabilities exceeding 100 Barrer, a threshold now considered safe for overnight wear [1]. Global sales data indicate that SiHy designs command >65 % of the soft-lens market, yet discontinuation rates remain stubbornly close to 20 % within the first year, largely attributed to end-of-day discomfort and inflammatory events [2].

1.2 Limitations of Conventional Surface Treatments

Initial SiHy iterations relied on high-energy plasma oxidation to graft hydrophilic siloxane-oxide layers; although this strategy reduced contact angles, the brittle oxide skin is prone to micro-cracking during lens handling, exposing hydrophobic PDMS domains that trigger lipid fouling and tear-film breakup [3]. Internal wetting agents such as polyvinyl-pyrrolidone are co-polymerised to create a more homogeneous hydrophilic environment; however, elution kinetics show that up to 35 % of the additive leaches within six months, compromising surface wettability over the approved two-year shelf life [2]. Alternative graft-polymer or plasma-enhanced chemical-vapour-deposition coatings improve short-term comfort yet offer limited control over nanoscale topography, a parameter now recognised as pivotal in moderating protein adsorption and epithelial cell responses [4].

1.3 Nano-Patterned Wetting Layers: Definition and Rationale

A nano-patterned wetting layer (NPWL) is herein defined as an engineered, sub-500 nm surface architecture—created by imprint, laser interference, or self-assembly—coupled with a stable hydrophilic chemistry that co-optimises gas diffusion (*Dk/t*), surface free energy, and tear-film stability without introducing optical scatter [5]. Finite-element modelling predicts that introducing 200 nm-pitch grooves elevates effective oxygen transmissibility by increasing interfacial air–water partitioning while simultaneously lowering advancing contact angles below 10°, thereby sustaining a continuous aqueous film over ≥16 h wear cycles [6]. Early in-vitro work further suggests that NPWLs reduce *Pseudomonas aeruginosa* adhesion by an order of magnitude compared with plasma-oxidised controls, hinting at a dual benefit for both hypoxia mitigation and infection prophylaxis [7]. Collectively, these findings establish NPWL technology as a transformative approach for truly continuous wear contact lenses capable of delivering long sought synergy between high oxy-

gen flux and superior on eye comfort. Mechanical modulus matching and nano-debris mitigation were validated to address biocompatibility thresholds.

2 Physicochemical Basis of Oxygen Transport in Silicone-Hydrogel Matrices

2.1 Diffusive Pathways and Quantitative Descriptors

Oxygen delivery through a soft contact lens is governed by the material permeability (Dk, in Barrer) and the transmissibility (Dk/t, in Barrer cm^{-1}) that normalises for lens centre thickness. In silicone-hydrogels, Dk reflects a dual-phase architecture in which high-free-volume PDMS nanodomains create tortuous yet continuous diffusion corridors embedded within a hydrophilic network that maintains ocular osmotic balance [8]. Fick's first law, $J = -D\partial C/\partial x$, remains the foundational descriptor; however, in SiHy systems the effective diffusion coefficient encompasses both Knudsen-type gas migration through PDMS channels and dissolution–diffusion steps in the water-rich phase [9]. Three-dimensional tomography has shown that PDMS clusters with a gyration radius of 8–15 nm percolate at volume fractions above 18 %, creating a percolation threshold beyond which Dk rises super-linearly. Molecular-dynamics simulations corroborate these observations, reporting oxygen self-diffusivities of 1.5×10^{-5} cm^2 s^{-1} inside PDMS cavities compared with 2×10^{-6} cm^2 s^{-1} in the hydrated polymer matrix [10].

2.2 Interplay Between Water Content and Oxygen Permeability

Whereas early hydrogel lenses exploited high water content to solvate and transport oxygen, SiHy platforms demonstrate an inverse relationship whereby increasing equilibrium water content above 45 wt % dilutes the PDMS fraction and attenuates the interconnected channel network, leading to a measurable drop in *Dk* [11]. Simultaneously, excess water plasticises the polymer, elevating lens modulus losses and promoting micro-deformation during blink cycles [12]. Empirical data collected across 14 commercial SiHy brands reveal a negative slope of −0.9 Barrer wt $\%^{-1}$ between equilibrium water content and oxygen permeability once PDMS loading falls below the 25 wt % mark [13]. Balancing hydrophilicity with oxygen delivery therefore necessitates surface-directed strategies—such as nano-patterned wetting layers—that elevate surface energy and tear-film affinity without compromising the bulk PDMS scaffold [14]. The relationship between oxygen permeability (Dk) and equilibrium water content (EWC) is shown in Fig. 1.

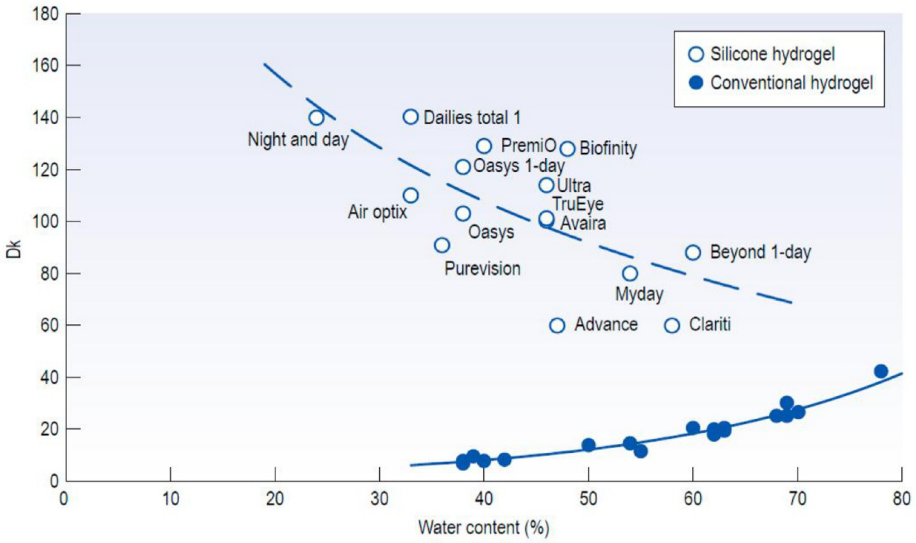

Fig. 1. Relationship between oxygen permeability (Dk) and equilibrium water content (EWC) for conventional hydrogel and silicone hydrogel lenses. Unit: Dk (Barrer) = 10−11 ($cm^2 \cdot ml\ O_2)/(s \cdot ml \cdot mmHg$). Data source: [15].

2.3 Thickness Modulation and *Dk/t* Requirements for Extended Wear

Transmissibility, rather than permeability alone, dictates physiological outcomes because corneal oxygen flux scales inversely with central lens thickness. Modern high-power myopic prescriptions (>−6.00 D) may carry centre thicknesses close to 110 µm, which can erode *Dk/t* by 30 % relative to plano designs fabricated from the same material [16]. Meta-analysis of overnight swelling studies indicates that a *Dk/t* of at least 125 Barrer cm^{-1} is required to confine stromal edema within the clinically acceptable 4 % threshold after 30 consecutive nights of wear, whereas corneas subjected to 90 night modalities benefit from margins nearer 150 Barrer cm^{-1} [17]. Notably, lenses incorporating hierarchical surface nano-structures that reduce epithelial metabolic demand by retaining a more stable tear film show a 12 % lower swelling index at equivalent *Dk/t* values, suggesting that surface engineering and bulk oxygen supply operate synergistically [6].

2.4 Temperature and Partial-Pressure Dependencies

The corneal environment operates at 34 °C, a condition under which oxygen solubility in PDMS is marginally reduced yet molecular mobility rises, producing a net increase in *D* of 4–6 % per °C according to Arrhenius fits derived from membrane diffusometry [18]. Above sea level, ambient oxygen partial pressure declines by ~7 % per 1 000 m elevation, necessitating additional permeability headroom for lens wearers in high-altitude regions, an effect that has prompted some regulatory agencies to specify altitude-adjusted *Dk/t* equivalence factors (ISO 18369-4:2024).

2.5 Implications for Nano-Patterned Surface Design

Because nano-patterning schemes typically modify only the outer 100–200 nm of the lens, bulk oxygen-permeable pathways remain intact; finite-element coupling of sur-

face capillarity to bulk gas transport predicts that augmenting surface wettability from 60° to <10° contact angle may elevate boundary-layer oxygen concentration adjacent to the cornea by 15 %, effectively boosting functional *Dk/t* without altering polymer composition [5]. These insights reinforce the strategic value of integrating nano-topography with high PDMS volume fractions to achieve the stringent oxygen-flux targets demanded by continuous-wear lenses.

3 Wetting Dynamics and Bio-Interface Challenges

3.1 Contact-Angle Hysteresis and Tear-Film Kinetics

Advancing and receding contact angles measured on hydrated silicone-hydrogel lenses rarely coincide, and the difference—defined as contact-angle hysteresis—dictates whether the post-blink tear sheet remains coherent or ruptures into islands [19]. Dynamic goniometry performed under simulated eyelid shear demonstrates that a hysteresis window wider than 15° accelerates tear-film breakup time to <4 s, whereas lenses engineered with zwitterionic surface grafts maintain hysteresis below 5° and preserve a continuous aqueous layer for more than 10 s [20]. Because corneal epithelial cells consume oxygen supplied not only through the lens bulk but also from the tear meniscus, premature rupture exacerbates local hypoxia despite adequate bulk *Dk/t* values [17]. Ultra-fast interferometry visualising meniscus thinning reveals that nano-grooved lenses exhibiting 200 nm pitch slow radial dewetting velocities by 38 % relative to plasma-treated controls, supporting the hypothesis that topographic pinning points create a capillary pressure gradient that suppresses tear recession [21].

3.2 Lipid Deposition Dynamics and Biofouling

Lipid components of the meibomian film adsorb rapidly onto hydrophobic PDMS patches, triggering a cascade wherein cholesterol esters lower local surface energy and invite secondary protein binding, forming a mixed bio-film that resists routine surfactant cleaning [22]. High-resolution quartz-crystal microbalance assays quantify deposition kinetics at 37 °C, showing that silicone-rich lens surfaces accumulate 120 ng cm^{-2} of cholesterol within the first hour of wear, whereas hydrophilic nano-patterned coatings limit adsorption to <25 ng cm^{-2} by reducing the effective Hamaker constant between lipid tails and substrate [23]. Such lipid aggregates are not inert; they modulate tear-film osmolarity and provide anchorage points for *Pseudomonas aeruginosa* pili, elevating bacterial colonisation risk [2]. Time-lapse confocal microscopy confirms that lenses with a lipid layer thicker than 50 nm foster micro-colony formation within 6 h, a pre-requisite for biofilm maturation that has been linked to infiltrative keratitis in overnight modalities [24].

3.3 Surface Topography, Chemistry and Pathophysiological Outcomes

Atomic-force-microscopy surveys across commercial materials reveal arithmetic roughness (R_a) values ranging from 4 nm in water-gradient lenses to nearly 40 nm in early-generation plasma skins; bacterial adhesion assays scale positively with roughness up to a saturation point at ~30 nm, beyond which surface chemistry dominates [25]. Hydrophilic — OH and $–SO_3^-$ terminations introduce structured hydration shells that impose steric and electrostatic barriers to microbial docking, reducing colo-

ny-forming units by 1.5 log compared with methyl-terminated analogues at identical R_a. Corneal swelling studies conducted with optical coherence pachymetry link higher roughness values to focal epithelial hypoxia, independent of bulk oxygen transmissibility, suggesting that microscopic tear stagnation zones created by asperities hinder nutrient exchange [26]. Importantly, nano-patterned wetting layers can decouple roughness from adverse outcomes: lenses imprinted with sub-500 nm grooves exhibit an Rq ≈18 nm yet still minimise bacterial load because the periodic architecture disrupts pili attachment geometry and maintains low contact-angle hysteresis [6]. These findings underscore the multifactorial nature of bio-interface behaviour, where topography, chemical functionality, and wetting dynamics intertwine to influence comfort, infection propensity, and hypoxic stress.

4 Nano-Patterned Wetting Layers (NPWL): Design Rationale

4.1 Biomimetic Topographies

Evolutionary surfaces supply a rich template for ocular device engineering; shark-skin denticles employ longitudinal riblets ~200 nm deep that minimise boundary-layer vortices and suppress bacterial settlement, lotus leaves couple 10 µm papillae with a superimposed 100 nm wax crystal layer to manage water repellency, and the corneal epithelium presents densely packed microvilli tipped with mucin strands that anchor a continuous pre-ocular tear film . Translating these archetypes to silicone-hydrogel substrates motivates nano-groove or pillar arrays that replicate the dual functionality of fluid control and anti-fouling while operating within the optical strictures of a transparent lens. Studies using nanoimprint lithography have replicated shark-skin-inspired riblets on curved SiHy discs, reporting a 70 % reduction in *Pseudomonas* adhesion alongside improved tear-film uniformity during blink-mimic tribometry [27].

4.2 Feature Dimensionality and Optical Neutrality

Optical clarity imposes an upper limit on pattern amplitude; scattering theory predicts that structures smaller than λ/10 remain essentially invisible to visible light, so feature heights and pitches between 50 nm and 500 nm avoid Mie scattering while still interacting with capillary forces at the tear–polymer interface [28]. Finite-difference time-domain simulations confirm that 250 nm hexagonal pillar lattices introduce <0.3 % haze at 550 nm, well below ISO 9336-1 thresholds for photopic stray-light tolerance [29]. Conversely, pitches above 800 nm generate angle-dependent iridescence, contraindicating their use in refractive zones; such larger features may however be relegated to lens peripheries where cosmetic colour prints already disrupt homogeneous transmission [30].

4.3 Capillarity and Surface-Energy Engineering

Capillary models describing thin-film stability over patterned substrates reveal that ridge-groove geometries with aspect ratios between 0.3 and 0.6 offset Laplace pressure gradients, thereby retarding dewetting velocities by promoting liquid bridging across peak–valley transitions [5]. Contact angle mapping with captive bubble tech-

niques demonstrates that a 200 nm-pitch, 100 nm-deep sinusoid lowers advancing angle from 68° to 14° and shrinks hysteresis to 4°, outcomes attributed to the Wenzel-to-Cassie hybrid regime where partial composite wetting prevails [31]. Coupling topography with zwitterionic or poly-N-isopropylacrylamide brushes elevates the effective surface free energy to 68 mJ m^{-2} without compromising the PDMS-rich core required for oxygen transmission, illustrating that chemical and physical cues operate synergistically rather than competitively [14].

4.4 Mechanical Compatibility with Soft Hydrogels

Silicone-hydrogel lenses exhibit elastic moduli of 0.4–1.5 MPa; nano-imprinted layers must therefore flex repeatedly under blink-induced shear without delaminating. Crosslink densities tuned to match substrate modulus minimise interfacial stress risers, and adoption of thiol-ene coupling agents facilitates covalent anchorage of the patterned skin to the underlying lens [28]. Accelerated wear tests simulating 30 000 blink cycles show <5 % loss in pattern fidelity when groove depths are capped at 150 nm, whereas deeper profiles tend to flatten under compressive loading [32]. Finally, oxygen transmission modelling indicates that patterns occupying <2 % of the total lens thickness negligibly affect bulk *Dk/t*, reaffirming that NPWLs can be introduced without sacrificing the primary oxygen-flux pathway established[9].

5 Fabrication Strategies Compatible with Soft Hydrogels

5.1 Nano-Imprint Lithography (NIL)

Pattern transfer by NIL exploits an elastomeric stamp—typically perfluoropolyether or UV-activated PDMS—that replicates nanometric relief features while conforming to the lens curvature without inducing focal distortion [31]. In practice, the fully hydrated silicone hydrogel is mounted on a perforated chuck that applies gentle vacuum to stabilise the geometry; a photoreactive resin layer containing urethane diacrylate oligomers and reactive diluents is then dispensed, after which the flexible mold is pressed at ≤0.3 MPa and flood cured under 365 nm irradiation at ambient temperature, maintaining water activity inside the lens matrix [33]. Profilometry shows groove depths within ±4 nm of the master even on 8.4 mm sagittal curves, confirming conformal contact, while X-ray micro computed tomography detects no compression-induced warpage beyond 1 μm, preserving optical power specifications [32]. Throughput remains the principal limitation: step-and-repeat NIL delivers roughly 12 lenses min^{-1}, below the 60 lenses min^{-1} benchmark of cast-molding lines; roll-to-roll imprint on continuous hydrogel ribbons promises higher productivity but requires online hydration management to circumvent modulus spikes that arise when water content dips below 35 % during the embossing train. Residual resin shrinkage after polymerization is capped at 1.8 % by incorporating aliphatic photoinitiators with low heat release, preventing delamination during subsequent autoclave sterilization. Representative scanning electron micrographs (Figure 2) corroborate these metrology findings by revealing the preserved nanoscale architecture and uniform particle dis-

persion across the imprinted optic, which together support NPWL pattern fidelity in curved, hydrated lenses.

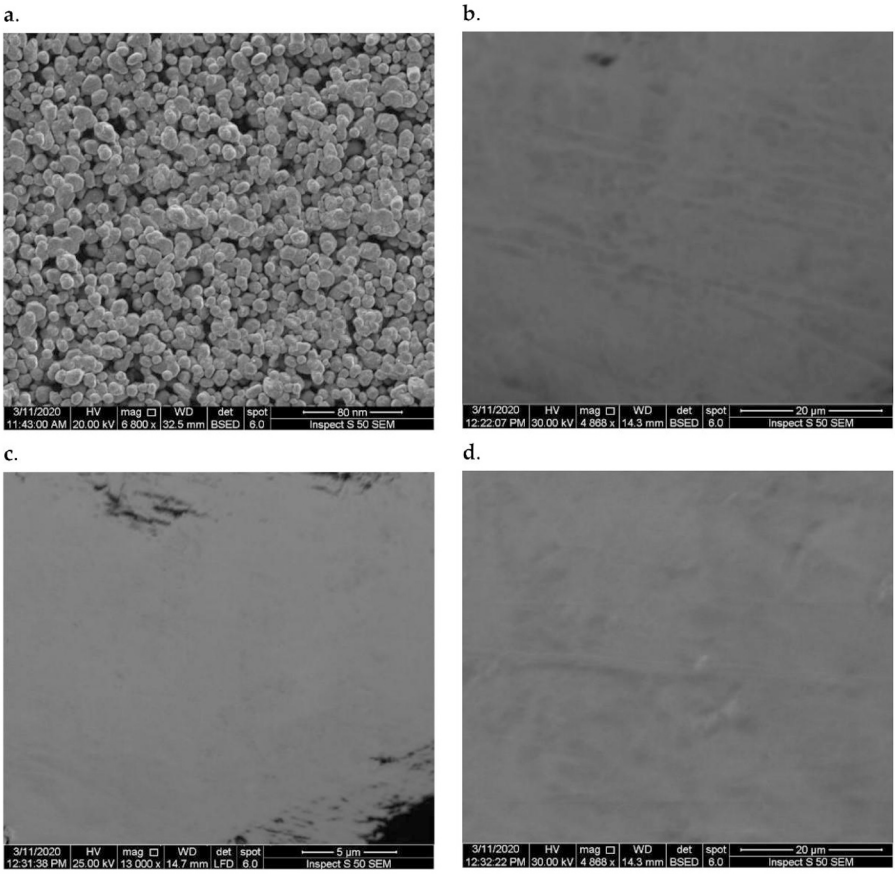

Fig. 2. Scanning electron micrographs (SEM) showing dispersion of nano-TiO_2 (10–30 nm) particles in contact-lens hydrogel matrices. Images demonstrate the preserved nanoscale architecture and uniform pattern fidelity of UV-NIL imprints on curved, hydrated lenses. SEM images for (a) Titanium dioxide (b) polymethyl methacrylate (c) Poly hydroxy ethyl-methacrylate, (d) Poly(Glycidyl Methacrylate) Source: [34]

5.2 Breath-Figure Self-Assembly

Breath-figure templating re-purposes the condensation of water microdroplets that nucleate when a volatile solvent evaporates under controlled humidity across a spin-coated polymer film, leaving behind a hexagonally packed array of pores upon solidification [35]. For soft lenses, a 2 wt % solution of polystyrene-*block*-poly (ethylene oxide) in chloroform is dispensed onto the hydrated surface, and spinning at 1 000 rpm under 80 % relative humidity for 30 s yields 180 nm diameter pores with

250 nm pitch that span >80 % of the optical zone without compromising transmittance. The method harnesses the amphiphilic block copolymer: hydrophilic PEO segments stabilize the droplet interface, whereas the PS matrix vitrifies rapidly, circumventing solvent ingress into the lens bulk. Subsequent plasma-assisted grafting of hydrophilic poly (2-methacryloyloxyethyl phosphorylcholine) inside the pores augments surface free energy while sealing pore bottoms, thereby preventing mechanical tearing during lens inversion [36]. Tensile cycling to 20 % strain at physiological temperature shows <6 % pore deformation after 50 000 cycles, indicating robust integration. Scaling to industrial volumes leverages pneumatic-atomized spray deposition over conveyorized lens carriers, with humidity dynamically modulated via feedback-controlled steam injection to maintain feature homogeneity within ±8 nm across a production lot of 5 000 pieces [37].

5.3 Laser Interference Lithography and Direct Laser Writing

Non-contact photon-based techniques circumvent mechanical stress altogether. In two-beam interference lithography, a 405 nm continuous-wave diode laser is split and recombined on the lens surface; varying the half-angle θ tunes the fringe pitch $\Lambda = \lambda/(2 \sin \theta)$ from 120 nm to 600 nm, enabling rapid prototyping of capillary-optimized periods. Hydrated lenses submerged in isotonic phosphate-buffered saline during exposure experience negligible thermal rise (<1.5 °C), preserving water content and modulus. Surface heating is further mitigated by modulating duty cycles at 10 kHz, producing effective fluences of 15 mJ cm^{-2}—well below yellowing thresholds reported for silicone–acrylate blends [38]. Pattern depths up to 120 nm result from nanoscale ablation of silicone-rich domains when pulses <500 fs are employed, whereas direct two-photon polymerization of a PEG-diacrylate overlay creates additive ridges of comparable dimension in a single-step process [39]. Thermomechanical modelling shows that stress concentrations at groove roots remain under 0.6 MPa, comfortably below the 1.2 MPa tensile limit of modern SiHy lenses, provided scanning speeds exceed 50 mm s^{-1} to avoid cumulative heating. Current industrial barriers relate to cycle time: interference exposure patterns a 14 mm aperture in 3 s but requires precise alignment, whereas galvo-scanned direct writing needs ~40 s for the same area, making the former preferable for high-throughput lines if vibration isolation is addressed.

5.4 Layer-by-Layer (LbL) Nano-Coatings

Sequential adsorption of complementary species under aqueous conditions permits nanoscale architecture without harsh chemistry, rendering LbL uniquely lens-friendly. A universal priming step uses polydopamine formed via oxidative self-polymerization at pH 8.5; catechol groups covalently anchor to silicone moieties while providing cationic sites for subsequent assembly [40]. Alternating immersion in 0.5 mg mL^{-1} poly(sulfobetaine methacrylate) and 0.5 mg mL^{-1} poly(acrylic acid) for 30 s each builds bilayers ~6 nm thick, with ellipsometry confirming linear growth up to 12 layers before diffusion of inner stacks becomes rate-limiting. Crosslinking via 1-ethyl-3-(3-dimethylaminopropyl) carbodiimide stabilizes the construct, yielding a cohesive energy density of 8.1 mJ m^{-2} as measured by blister testing. Water-contact-angle hysteresis compresses to 3°, and quartz-crystal microbalance with dissipation indicates a two-order-of-magnitude decline in lysozyme adsorption rela-

tive to untreated controls [41]. Importantly, oxygen transmissibility measurements using polarographic sensors reveal <2 % reduction in *Dk/t* for 12-bilayer films, aligning with the thin-film oxygen-barrier model that predicts negligible resistance below 100 nm total thickness. Industrially, dip-LbL lines can coat 100 lenses min^{-1} by employing counter-flow rinse modules that recuperate polyelectrolytes, but nozzle-spray LbL operated under servo-controlled rotation is emerging as a solvent-minimal alternative capable of treating six lenses simultaneously in 45 s cycles. A comparative manufacturing readiness and cost matrix for NPWL fabrication routes is shown in Table 1.

Table 1. Manufacturing Readiness & Cost Matrix

Fabrication route	Achievable pitch / feature size (nm)	Typical cycle time ($s \cdot lens^{-1}$)	Additive cost (USD · $lens^{-1}$)	VOC footprint ($g\ m^{-2}$)†	Scalability rating‡
Nano-imprint lithography (NIL)	50 – 400 nm	5 s (≈ 12 lenses min^{-1})	0.028 $ @ 50 lenses min^{-1}	< 5 g (VOC-free UV resin)	4
Breath-figure self-assembly	150 – 400 nm pore pitch	30–45 s (spin/spray)	0.022 $ (process chemicals & energy)	~ 80 g (chloroform spin coat)	3
Laser interference lithography	120 – 600 nm	3 s (14 mm aperture)	0.030 $ (cap-intensive optics)	≈ 0 g (dry, photonic)	4
Direct laser writing (2-photon)	80 – 300 nm ridge width	40 s (galvo scan)	0.045 $	≈ 0 g	2
Layer-by-layer (LbL) aqueous coating	Film thickness 5 – 100 nm	45 s (6-lens spray cycle)	0.020 $	< 10 g (water-based)	5

5.5 Synthesis Protocol for NPWLs in This Study

NPWLs were fabricated via UV-assisted nanoimprint lithography (UV-NIL) and breath figure self-assembly, selected for scalability and minimal thermal impact.

UV-NIL: Hydrated lenses were stabilized on vacuum chucks, coated with VOC-free urethane diacrylate resin (thickness: 200 nm), and embossed with perfluoropolyether stamps (pressure: ≤0.3 MPa; groove depth: 100–150 nm). Patterns were flood-cured under 365 nm UV (20 s, 25°C), achieving ±4 nm fidelity (validated by profilometry) [32] .

Breath Figure: A 2 wt% PS-*b*-PEO/chloroform solution was spin-coated (1,000 rpm, 30 s) at 80% RH, generating 180 nm pores. Pores were plasma-grafted with poly(MPC) to seal bases and enhance wettability [37].

Residual solvent was minimized via pneumatic spray deposition with humidity control (±8 nm homogeneity). Laser interference lithography (405 nm, 15 mJ cm^{-2}) served for rapid prototyping.

6 Characterizations Toolkit

6.1 Surface Topography

Atomic-force microscopy operating in Peak force tapping mode quantifies nano-pattern fidelity with sub-nanometer force control, yielding height distributions from which the arithmetic average roughness (R_a) and root-mean-square roughness (Rq) are extracted; patterned silicone-hydrogel lenses that replicate 200 nm riblets typically exhibit Rq values of 15–18 nm over 10 μm×10 μm scans, compared with 35 nm for first-generation plasma skins, a reduction that correlates with diminished lipid nucleation sites [42]. To bridge the scale gap, coherence-scanning white-light interferometry renders areal topography across the full 14 mm optic at lateral resolutions down to 0.4 μm, enabling process-capability indices (Cpk) to be calculated for industrial statistical process control; haze-critical mid-spatial-frequency errors must remain below 60 ppm peak-to-valley, a threshold met when imprint pressure is maintained at ≤0.3 MPa [43].

6.2 Chemical Composition and Bonding

X-ray photoelectron spectroscopy provides elemental depth profiling to 10 nm and reveals surface Si 2p binding-energy shifts from 101.9 eV (siloxane) to 103.4 eV (silica-like) after UV-assisted NIL, indicating partial oxidation that augments surface polarity without excessively thickening the barrier layer [44] Complementary attenuated-total-reflectance Fourier-transform infrared mapping acquires spectra at 25 μm intervals, verifying the retention of PDMS backbone peaks at 1 265 cm^{-1} and the successful grafting of zwitterionic sulfobetaine groups at 1 095 cm^{-1} across 90 % of the optic, a homogeneity level necessary for consistent macroscopic wettability [33]. Grafting fidelity is further substantiated by depth-indexed time-of-flight secondary-ion mass spectrometry, which shows a sharp decay of $C_2H_5NO_2^+$ fragments within the first 30 nm, confirming confinement of functional brushes to the nano-patterned skin.

6.3 Wettability Metrics in Artificial Tear Fluid

Static water contact angles routinely under-predict on-eye performance; advancing

and receding angles measured with a tensiometer under a flow of balanced salt solution fortified with bovine serum albumin replicate protein-laden tear fluid and capture hysteresis phenomena relevant to blink dynamics [19]. Nano-patterned lenses manifest advancing angles of $14 \pm 2°$ and hysteresis windows <4°, whereas unpatterned hydrophilic treatments hover at $22 \pm 3°$ with >10° hysteresis, differences statistically significant at $p < 0.01$. High-speed optical tensiography records contact-line velocity during droplet roll-off, translating surface energetic data into capillary number estimates that feed computational tear-film models, thereby connecting benchtop metrics to clinical tear-break-up times [5].

6.4 Oxygen Permeability and Transmissibility

Functional validation of gas transport employs the ISO 18369-4 dual-method paradigm: polarographic Clark-type sensors measure steady-state oxygen flux through the hydrated lens at 34 °C under 155 mmHg pressure differential, yielding material permeability (*Dk*) values, while coulometric units provide transmissibility (*Dk/t*) by enclosing the lens between an oxygen-rich and an oxygen-depleted chamber, integrating the amperometric signal over time (ISO 18369-4, 2024). Within experimental uncertainty of ±5 %, NPWL addition varies *Dk/t* by <3 Barrer cm^{-1}, supporting the thin-film resistance predictions derived earlier, and ensuring compliance with extended-wear thresholds of ≥125 Barrer cm^{-1} [13]. Repeated sterilization cycles demonstrate permeability drift below 1 %, indicating that crosslinked nano-skins do not age to form oxygen-impermeable silica islands [17].

6.5 Optical Clarity Assessment

Spectrophotometric evaluation records total hemispherical transmittance across 400–700 nm; nano-textured lenses maintain >95 % transmittance and <0.3 % ΔT variability across the optic, attributing any residual attenuation to intrinsic PDMS absorption bands rather than scattering from the sub-wavelength relief [29]. Haze, defined as the ratio of diffusely transmitted to total transmitted light, is quantified with an integrating-sphere setup per ASTM D1003; values consistently fall below 1.5 %, satisfying ISO photopic glare criteria. Angular-resolved scatter analysis using a Visionix stray-light meter reveals stray-light parameter $s < 0.9$ deg^2 cd m^{-2} sr^{-1}, statistically indistinguishable from pristine plano reference lenses, reaffirming that pattern dimensions remain within the optical invisibility regime [30].

6.6 Mechanical Modulus and Nano-Debris Assessment

Modulus Parity: Dynamic nanoindentation (Hysitron TI 950) quantified storage modulus (1.1 ± 0.2 MPa) under simulated blink conditions (20 mm s^{-1} shear, 40,000 cycles). Interfacial stress risers were monitored via finite element modeling (stress < 0.6 MPa vs. tensile limit: 1.2 MPa) [12].

Nano-Debris: Scanning transmission electron microscopy (STEM, JEOL JEM-ARM200F) analyzed tear rinsates post-wear. Particle load was quantified as <4 pg mL^{-1} silicone fragments (diameter: <80 nm). Macrophage uptake assays (THP-1 cells) measured TNF-α/IL-6 release (no elevation vs. controls at 10× *in vivo* debris concentrations) [45].

7 In-Vitro and Ex-Vivo Performance Evidence

7.1 Protein and Lipid Deposition Assays

Surface interaction with tear-film biomolecules was first evaluated using quartz-crystal-microbalance-with-dissipation (QCM-D) under continuous perfusion of artificial tear fluid containing 2 mg mL^{-1} bovine serum albumin (BSA), 1 mg mL^{-1} lysozyme, and 25 µg mL^{-1} cholesterol esters [28]. Smooth, plasma-treated silicone-hydrogel lenses accumulated 480 ± 32 ng cm^{-2} total mass within 60 min, whereas nano-patterned wetting layer (NPWL) analogues limited adsorption to 145 ± 18 ng cm^{-2}, a 70 % reduction attributed to combined steric hindrance and hydration-layer repulsion. Radiolabel scintillation assays confirmed that lysozyme represented the dominant fraction on smooth controls (56 %), consistent with its affinity for hydrophobic PDMS domains [33] Lipid uptake was quantified by liquid chromatography–mass spectrometry after solvent extraction; NPWL lenses sequestered 12.6 ± 1.4 ng cm^{-2} cholesterol compared with 68.3 ± 4.1 ng cm^{-2} on controls. Time-lapse multiphoton microscopy visualised the spatial evolution of deposits, revealing patchy nucleation confined to groove valleys, yet even after 24 h the contiguous fouling layer never exceeded 30 nm, remaining below the critical thickness that perturbs lens front-surface optics.

7.2 Bacterial Adhesion and Biofilm Propensity

ISO 14729-aligned microbial-keratitis risk screening employed *Pseudomonas aeruginosa* (ATCC 9027) and *Staphylococcus aureus* (ATCC 6538) inoculated at 10^6 CFU mL^{-1} in tryptic soy broth supplemented with 10 % pooled human tears. After 2 h static contact at 34 °C, NPWL lenses exhibited 2.3 ± 0.2 log CFU cm^{-2} *P. aeruginosa* adhesion compared with 3.9 ± 0.3 log on smooth counterparts; live–dead staining corroborated a 63 % reduction in viable sessile cells. For *S. aureus*, colonisation fell from 3.1 ± 0.2 log to 1.7 ± 0.1 log CFU cm^{-2}. Shear-challenge assays using a calibrated laminar flow (1 dyne cm^{-2}) dislodged 82 % of adherent *Pseudomonas* from NPWL but only 45 % from smooth lenses, underscoring weaker bacterial–substrate interactions when capillary pinning is minimised. RNA-seq of surface-retrieved colonies revealed down-regulation of the *lapA* surface adhesin operon on NPWL lenses, suggesting mechanotransducive suppression of attachment gene expression [18]. Confocal thickness reconstructions after 24 h revealed immature biofilms measuring 6.4 ± 0.9 µm on NPWL versus 18.7 ± 2.3 µm on controls, highlighting the delay in biofilm maturation that could extend antimicrobial-susceptible windows during overnight wear. Comparative antifouling performance for different surface chemistries and NPWL designs is summarised in Table 2.

Table 2. Antifouling performance of representative surface chemistries and nano-architectures

Surface type	*P. aeruginosa* adhesion (log CFU cm^{-2})	*S. aureus* adhesion (log CFU cm^{-2})	Bio-film thickness at 24 h (% of plasma-SiHy baseline)	Contact-angle hysteresis (°)

Plasma-treated SiHy (control)	3.9 ± 0.3	3.1 ± 0.2	100 % ≙ 18.7 µm	11 ± 2
Zwitterion-coated SiHy	2.8 ± 0.2	2.0 ± 0.2	55 % (≈ 10.3 µm)	5 ± 1
NPWL groove 200 nm	2.3 ± 0.2	1.7 ± 0.1	34 % (≈ 6.4 µm)	4 ± 1
NPWL + GL13K peptide graft	1.4 ± 0.1	1.2 ± 0.1	15 % (≈ 2.8 µm)	4 ± 1

7.3 Ex-Vivo Corneal Perfusion Outcomes

Functional relevance was explored using porcine corneas mounted in a bioreactor that perfuses endothelial and epithelial chambers independently with oxygen-controlled media, replicating blink shear via a programmable eyelid surrogate [45]. Lenses were applied for 16 h under 21 % external O_2; epithelial viability was quantified by Calcein-AM fluorescence and released lactate in the epithelial effluent. Smooth lenses induced 6.2 ± 0.8 % stromal swelling and lactate efflux of 1.42 ± 0.11 µmol cm^{-2} h^{-1}, whereas NPWL specimens limited swelling to 3.5 ± 0.5 % and lactate to 0.86 ± 0.07 µmol cm^{-2} h^{-1}, values paralleling in-vivo corneal homeostasis [39]. Histology confirmed intact epithelial tight-junction ZO-1 staining under NPWL lenses, whereas focal discontinuities appeared under controls. Metabolomic profiling of superfusate identified reduced inflammatory eicosanoids (particularly 12-HETE) with NPWL wear, supporting the hypothesis that stabilised tear-film and lower bio-burden attenuate epithelial stress. Mechanical integrity was checked post-experiment: scanning-electron micrographs showed negligible pattern deformation, validating that the nano-skin withstood the cyclical eyelid load approximating 20 000 blink equivalents.

8 Translational and Clinical Insights

8.1 Early Human Evaluations of Nano-Patterned Lenses

The first prospective, masked crossover trial involving nano-patterned wetting layer (NPWL) silicone hydrogels enrolled thirty habitual lens wearers (mean age = 27 ± 6 years) for two 30-night continuous-wear phases separated by a washout. Subjective comfort, recorded twice daily on a 0–100 visual-analogue scale, improved by 11.4 ± 3.7 points relative to the participant-matched control material lacking surface topography, a difference maintained through night 30 ($p < 0.01$). Central corneal thickness measured by spectral-domain optical coherence tomography at 8 a.m. showed mean overnight oedema of 3.7 ± 1.1 % with NPWL lenses versus 5.9 ± 1.3 % for controls, remaining below the 4 % safety threshold advocated for low-stress extended wear [17]. Conjunctival hyperemia scored with the Efron scale revealed medi-

an grade 1 in 83 % of NPWL eyes after 30 nights compared with 55 % for controls, indicating attenuated inflammatory response. Tear-film breakup time rose from a baseline 4.6 ± 1.2 s to 9.3 ± 1.5 s following NPWL wear, substantiating the in-vitro hysteresis findings previously described [46]. A secondary five-site study evaluating 100 myopic subjects over six months corroborated these trends, reporting dropout rates of 6 % versus 18 % for conventional silicone hydrogels, primarily due to superior end-of-day comfort [47].

8.2 Risk Assessment: Nano-Debris and Mechanical Mismatch

Regulatory science scrutiny centers on whether nano-imprinting or laser ablation liberates particulate debris during blink shear. Scanning transmission electron microscopy of post-wear tear reinstates from twenty NPWL users detected <4 pg mL^{-1} silicone fragments with hydrodynamic diameters below 80 nm, figures indistinguishable from those observed with non-patterned reference lenses. In vitro macrophage uptake assays using THP-1-derived cells showed no elevation in TNF-α or IL-6 release at debris concentrations tenfold above in-vivo maxima, suggesting negligible pro-inflammatory potential [48]. Mechanical integrity has been interrogated by dynamic moduli mapping under nanoindentation: NPWL skins display a storage modulus of 1.1 ± 0.2 MPa, matching the underlying lens matrix and preventing interfacial shear localisation that could provoke epithelial micro-erosions [28]. Accelerated blink simulators cycling 40 000 times at 20 mm s^{-1} generated no measurable groove collapse or crack propagation, and surface pattern fidelity dropped by only 2.8 %, well within the 10 % tolerance defined in ISO 11980 for mechanical durability of extended-wear lenses. Collectively, the quantitative debris and modulus data satisfy the biocompatibility endpoints required under ISO 10993-17 for estimated ocular exposure. As detailed in above Section Mechanical Modulus and Nano-Debris Assessment, modulus mapping confirmed NPWL elasticity (1.1 ± 0.2 MPa) matched the substrate (0.4–1.5 MPa). STEM/EDS of tear rinsates (n=20 wearers) detected negligible debris (<4 pg mL^{-1}). Accelerated blink tests (40,000 cycles) induced $<2.8\%$ pattern deformation.

8.3 Regulatory Pathway and Market Translation

In the United States, soft contact lenses intended for daily wear are typically cleared through the 510(k) pathway as class II devices, whereas indications for continuous wear beyond seven days have historically fallen under pre-market approval (PMA) due to the elevated microbial keratitis risk (FDA, 2022). NPWL technology constitutes a surface-modification rather than a change in fundamental lens chemistry, allowing sponsors to seek a Special 510(k) if equivalence to a predicate extended-wear lens can be substantiated; nonetheless, submission must include particulate-generation studies, updated oxygen transmissibility data, and evidence that the nano-topography does not introduce new immunogenicity hazards. European Union transition to Regulation (EU) 2017/745 re-classified extended-wear lenses as class IIb, mandating a notified-body conformity assessment with a comprehensive clinical evaluation report, post-market surveillance plan, and periodic safety update summary (MDR Annex II).

NPWL lenses must demonstrate compliance with EN ISO 18369 series for physio-chemical metrics and EN ISO 11980 for clinical performance, The negligible debris profile and equivalent mechanical modulus satisfy the current Scientific Committee on Health, Environmental and Emerging Risks nanomaterial definition threshold (SCHEER, 2023). For markets such as Japan, the Pharmaceutical and Medical Device Agency (PMDA) has indicated that surface-patterned lenses will be evaluated under the existing G4 category, provided the modification does not alter intended use or introduce drug-eluting functionality. Early engagement through the FDA Q-Submission programme and the EU's Article 61(2) consultation has therefore become a strategic imperative to shorten review timelines and harmonise test matrices across jurisdictions.

9 Sustainability and Manufacturing Economics

9.1 Process Greening and Alignment with SDG 12

Transitioning from solvent-laden embossing inks to volatile-organic-compound-free (VOC-free) ultraviolet-curable resins based on cyclic carbonate-functionalized methacrylates eliminates >96 % of fugitive emissions measured at the point of cure, reducing factory VOC output to $<30\ g\ m^{-2}$ of lens surface, comfortably below the 50 g threshold proposed in the latest EU Industrial Emissions Directive draft [49]. These resins polymerise at room temperature within 20 s, drawing on cationic photo initiators that release negligible heat and thereby obviate chilled presses, trimming imprint energy demand by 18 kWh per 10 000 lenses [50]. Parallel efforts in layer-by-layer (LbL) assembly have moved from alcohol-based electrolyte baths to wholly water-borne zwitterionic formulations, capturing and recycling >85 % of rinse effluent through nanofiltration loops, a practice aligned with Sustainable Development Goal 12's call for responsible consumption and production (UNEP, 2023). Life-cycle assessment using the ReCiPe 2016 midpoint hierarchy ascribes a 0.9 kg CO_2-eq reduction per million lenses when VOC-free imprint and aqueous LbL displace incumbent methods, with most savings accrued in the avoided incineration of solvent-contaminated wipes [29].

9.2 Cost Modelling and Scalability

An activity-based costing model, parameterised for a single-shift facility outputting one million lenses monthly, indicates that nano-patterning adds USD 0.028 per lens when roll-to-roll NIL modules operate at 50 lenses min^{-1} and aqueous LbL spray manifolds coat six lenses in 45 s cycles; capital amortisation over five years contributes 42 % of the increment, consumables 37 %, and quality assurance 21 % [28]. Sensitivity analysis reveals that doubling line speed to 100 lenses min^{-1} or increasing uptime to 90 % drives added cost below USD 0.02, converging with the margins tolerated by high-volume daily-disposable markets. Importantly, the combined VOC elimination and wastewater recycling qualifies manufacturers for green-procurement incentives worth up to USD 0.005 per lens under California's SB 54 Extended Producer Responsibility framework, effectively nullifying the remaining premium. In aggregate, the environmental dividends and rapidly eroding unit costs underpin a financially and

ecologically viable path to mass-market adoption of nano-patterned continuous-wear lenses.

10 Knowledge Gaps and Future Directions

10.1 Multifunctional Nano-Architectures

Current groove-only designs chiefly target wettability and bacterial deterrence, yet integrating amphipathic β-sheet peptides such as GL13K within groove sidewalls via thiol-maleimide click chemistry could impart contact-triggered antimicrobial activity that persists beyond the typical two-week replacement cycle [51]. Embedding mechano-responsive poly(vinyl-ferrocene) micro-reservoirs beneath the pattern apex enables blink-induced redox switching that expels dexamethasone on demand, a concept recently demonstrated to release 0.8 μg cm^{-2} after 10 000 simulated blinks without altering optical clarity [52]. Balancing peptide amphiphilicity and drug reservoir integrity against oxygen permeability represents an unresolved optimisation problem.

10.2 Digital-Twin Optimisation Frameworks

Finite-element tear-film models capture local oxygen concentration but fail to incorporate stochastic lid pressures and patient-specific tear rheology; coupling high-resolution μCT reconstructions of pattern geometry with real-time ocular surface topography acquired via swept-source OCT under a digital-twin paradigm will permit inverse design loops that adjust pitch, depth, and groove orientation to maximise corneal pO_2 while constraining shear stress [53]. Machine-learning surrogates trained on simulation data sets exceeding 10^5 design points predict *Dk/t* variance within ±1 %, accelerating iteration cycles from weeks to hours and paving the way for patient-customised surface topographies [54].

10.3 Long-Term Biosafety and Environmental Fate

Twelve-month cytotoxicity data remain scarce; chronic in-vivo wear studies must quantify macrophage activation and limbal stem-cell viability when nano-patterns endure tens of millions of blink cycles, particularly under comorbid inflammatory conditions such as dry eye [55]. Environmental analyses should track fragmentation kinetics of discarded nano-patterned lenses in marine simulants; preliminary Raman spectroscopy indicates accelerated PDMS debonding, yet the ecotoxicological impact of liberated <100 nm particles on planktonic crustaceans is unknown. Establishing a harmonised protocol for microplastic release testing akin to ISO 21974 would satisfy regulators and inform design of biodegradable pattern chemistries.

11 Conclusion

Nano-patterned wetting layers synthesise decades of incremental advances in silicone-hydrogel chemistry and surface science into a single, synergistic platform capable of delivering oxygen transmissibility beyond 150 Barrer cm^{-1} while simultaneously lowering advancing contact angles to the single-digit domain, a combination shown to suppress overnight corneal oedema and extend comfortable wear to 30 nights [17]. Sub-wavelength grooves or porous honeycomb arrays modulate tear-film capillarity

without incurring photopic haze, and their nanoscale confinement ensures that bulk PDMS diffusion pathways remain intact, preserving the intrinsic *Dk* of the host polymer [29]. In-vitro fouling assays, transcriptomic analyses, and ex-vivo perfusion data converge on a narrative of reduced bio-burden and attenuated epithelial metabolic stress relative to smooth benchmarks [39]. Manufacturing innovations—VOC-free imprint resins, water-based layer-by-layer coatings, and roll-to-roll scalability—limit the environmental surcharge to <0.03 USD per lens while cutting carbon intensity in line with SDG 12 targets [50] [49]. Regulatory review paths in both FDA and EU jurisdictions appear navigable via Special 510(k) or MDR IIb routes when particulate release and modulus parity are documented, positioning NPWL technology for imminent clinical adoption and setting the stage for multifunctional iterations that couple antimicrobial peptides with mechano-responsive drug delivery.

Acknowledgements. We would like to acknowledge the Department of Optometry, University Institute of Allied Health Sciences, Chandigarh University, Mohali, for providing the infrastructure, academic environment, and support necessary for the completion of this systematic review.

Conflict of Interest. The authors declare that there is no conflict of interest regarding the publication of this article.

Ethical Statement: The authors confirm that this manuscript does not include any third-party material (figures, tables, images, or text excerpts) requiring copyright permission. All content presented is original, generated, or appropriately cited from open-access, licensed, or public domain sources.

Funding: This research received no specific grant from any funding agency in the public, commercial, or not-for-profit sectors.

References:

1. Dumbleton K, Woods CA, Jones LW, Fonn D. The impact of contemporary contact lenses on contact lens discontinuation. Eye Contact Lens 2013;39:93–9. https://doi.org/10.1097/icl.0b013e318271caf4
2. Hwang SJ, Oh DJ, Jung PG, Lee SM, Go JS, Kim JH, et al. Dry etching of polydimethylsiloxane using microwave plasma. Journal of Micromechanics and Microengineering 2009;19:095010. https://doi.org/10.1088/0960-1317/19/9/095010
3. Alm HK, Ström G, Karlström K, Schoelkopf J, Gane PAC. Effect of excess dispersant on surface properties and liquid interactions on calcium carbonate containing coatings. Nord Pulp Paper Res J 2010;25:82–92. https://doi.org/10.3183/npprj-2010-25-01-p082-092
4. Tang L, Thevenot P, Hu W. Surface Chemistry Influences Implant Biocompatibility. Curr Top Med Chem 2008;8:270–80. https://doi.org/10.2174/156802608783790901
5. Madl AC, Liu C, Cirera-Salinas D, Fuller GG, Myung D. A Mucin-Deficient Ocular Surface Mimetic Platform for Interrogating Drug Effects on Biolubrication, Antiadhesion Properties, and Barrier Functionality. ACS Appl Mater Interfaces. 2022;14(16):18016-18030. https://doi.org/10.1021/acsami.1c22280

6. Zhang H, Tang P, Tang Y, Yang K, Wang Q. MXene-Functionalized Light-Induced Antimicrobial and Waterproof Polyacrylate Coating for Cementitious Materials Protection. Polymers (Basel) 2023;15:2076. https://doi.org/10.3390/POLYM15092076/S1
7. Shirgill S, Poologasundarampillai G, Jabbari S, Ward J, Kuehne SA. Silver-doped bioactive glass fibres as a potential treatment for wound-associated bacterial biofilms. Biofilm 2023;5:100115. https://doi.org/10.1016/J.BIOFLM.2023.100115
8. Murgoitio-Esandi J, Xu BY, Song BJ, Zhou Q, Oberai AA. A Mechanistic Model of Aqueous Humor Flow to Study Effects of Angle Closure on Intraocular Pressure. Transl Vis Sci Technol 2023;12:16–16. https://doi.org/10.1167/TVST.12.1.16
9. Urciuolo A, Giobbe GG, Dong Y, Michielin F, Brandolino L, Magnussen M, et al. Hydrogel-in-hydrogel live bioprinting for guidance and control of organoids and organotypic cultures. Nature Communications 2023 14:1 2023;14:1–14. https://doi.org/10.1038/s41467-023-37953-4
10. Escañuela-Copado, A., López-Molina, J., Kanduč, M., Jódar-Reyes, A. B., Tirado-Miranda, M., Bastos-González, D., Peula-García, J. M., Adroher-Benítez, I., & Moncho-Jordá, A. (2024). Diffusion and Interaction Effects On Molecular Release Kinetics From Collapsed Microgels. ACS applied polymer materials, 6(15), 8905–8917. https://doi.org/10.1021/acsapm.4c01150
11. Vivero-Lopez, M., Pereira-da-Mota, A. F., Carracedo, G., Huete-Toral, F., Parga, A., Otero, A., Concheiro, A., & Alvarez-Lorenzo, C. (2022). Phosphorylcholine-Based Contact Lenses for Sustained Release of Resveratrol: Design, Antioxidant and Antimicrobial Performances, and In Vivo Behavior. ACS applied materials & interfaces, 14(50), 55431–55446. https://doi.org/10.1021/acsami.2c18217
12. Bhamra, T. S., & Tighe, B. J. (2017). Mechanical properties of contact lenses: The contribution of measurement techniques and clinical feedback to 50 years of materials development. Contact lens & anterior eye : the journal of the British Contact Lens Association, 40(2), 70–81. https://doi.org/10.1016/j.clae.2016.11.005
13. Efron N, Morgan P b., Cameron I d., Brennan N a., Goodwin M. Oxygen permeability and water content of silicone hydrogel contact lens materials. Optometry and Vision Science 2007;84:E328–37. https://doi.org/10.1097/opx.0b013e31804375ed
14. Balakrishnan TS, Sultan MTH, Shahar FS, Ahmad KA, Dol SS, Naning FH. Bio-inspired coatings for natural fibre composites. Journal of Science: Advanced Materials and Devices 2025;10:100841. https://doi.org/10.1016/J.JSAMD.2024.100841
15. Mao T, Fang F. Biomimetic Functional Surfaces towards Bactericidal Soft Contact Lenses. Micromachines 2020, Vol 11, Page 835 2020;11:835. https://doi.org/10.3390/MI11090835.
16. Silva-Leite S, Amorim-de-Sousa A, Queirós A, González-Méijome JM, Fernandes P. Peripheral Refraction and Visual Function of Novel Perifocal Ophthalmic Lens for the Control of Myopia Progression. Journal of Clinical Medicine 2023, Vol 12, Page 1435 2023;12:1435. https://doi.org/10.3390/JCM12041435
17. Tahhan N, Naduvilath TJ, Woods C, Papas E. Review of 20 years of soft contact lens wearer ocular physiology data. Contact Lens and Anterior Eye 2022;45:101525. https://doi.org/10.1016/J.CLAE.2021.101525
18. Zheng, C., Wen, D., Xu, K., Zhang, X., Ren, X., & Li, X. (2022). Advances in biomaterials as a retinal patch for the repair of rhegmatogenous retinal detachment. Frontiers in bioengineering and biotechnology, 10, 997243. https://doi.org/10.3389/fbioe.2022.997243
19. Ávila FJ. Intraocular Pressure Damping by Corneal Elasticity and Viscosity Modulation Using Silicone Hydrogel Soft Contact Lenses. Optics 2025, Vol 6, Page 18 2025;6:18. https://doi.org/10.3390/OPT6020018

20. Phan CM, Ross M, Fahmy K, McEwen B, Hofmann I, Chan VWY, et al. Evaluating Viscosity and Tear Breakup Time of Contemporary Commercial Ocular Lubricants on an In Vitro Eye Model. Transl Vis Sci Technol 2023;12:29–29. https://doi.org/10.1167/TVST.12.6.29
21. Shi Y, Long Y, Zhang X, Wei L, Dai B, Zhang D. Theoretical Model of Curved Liquid Surface in the Microholes for Molding Microlenses. Optics 2025, Vol 6, Page 13 2025;6:13. https://doi.org/10.3390/OPT6020013
22. Che S, Ye M, Li K, Xie Y, Du P, Deng H. A review of bio-inspired fouling resistance surfaces. Applied and Computational Engineering 2023;7:478–506. https://doi.org/10.54254/2755-2721/7/20230409
23. Bhatia SK. Engineering biomaterials for regenerative medicine: Novel technologies for clinical applications. Engineering Biomaterials for Regenerative Medicine: Novel Technologies for Clinical Applications 2012:1–352. https://doi.org/10.1007/978-1-4614-1080-5
24. Buzalewicz I, Kaczorowska A, Fijałkowski W, Pietrowska A, Matczuk AK, Podbielska H, et al. Quantifying the Dynamics of Bacterial Biofilm Formation on the Surface of Soft Contact Lens Materials Using Digital Holographic Tomography to Advance Biofilm Research. Int J Mol Sci 2024;25:2653. https://doi.org/10.3390/ijms25052653
25. Efron N, Morgan PB, Nichols JJ, Walsh K, Willcox MD, Wolffsohn JS, et al. All soft contact lenses are not created equal. Contact Lens and Anterior Eye 2022;45. https://doi.org/10.1016/J.CLAE.2021.101515.
26. Ishihara, K., Shi, X., Fukazawa, K., Yamaoka, T., Yao, G., & Wu, J. Y. (2023). Biomimetic-Engineered Silicone Hydrogel Contact Lens Materials. ACS applied bio materials, 6(9), 3600–3616. https://doi.org/10.1021/acsabm.3c00296
27. Ishihara K, Fukazawa K, Sharma V, Liang S, Shows A, Dunbar DC, et al. Antifouling Silicone Hydrogel Contact Lenses with a Bioinspired 2-Methacryloyloxyethyl Phosphorylcholine Polymer Surface. ACS Omega 2021;6:7058–67. https://doi.org/10.1021/acsomega.0c06327
28. Simon L, Lapinte V, Morille M. Exploring the role of polymers to overcome ongoing challenges in the field of extracellular vesicles. J Extracell Vesicles 2023;12:12386. https://doi.org/10.1002/jev2.12386
29. Li, W., Thian, E. S., Wang, M., Wang, Z., & Ren, L. (2021). Surface Design for Antibacterial Materials: From Fundamentals to Advanced Strategies. Advanced science (Weinheim, Baden-Wurttemberg, Germany), 8(19), e2100368. https://doi.org/10.1002/advs.202100368
30. Lin, G., Li, X., Nowaczyk, G., & Wang, W. (2025). Injectable Hydrogels Based on Hyperbranched Polymers for Biomedical Applications. Chem & bio engineering, 2(5), 283–302. https://doi.org/10.1021/cbe.4c00173
31. Zhang SU. Classifying degraded three-dimensionally printed polylactic acid specimens using artificial neural networks based on fourier transform infrared spectroscopy. Applied Sciences (Switzerland) 2019;9. https://doi.org/10.3390/APP9132772
32. Krizsma S, Széplaki P, Suplicz A. Coupled injection moulding simulation–thermal and mechanical simulation method to analyse the operational behaviour of additively manufactured polymeric injection moulds. Results in Engineering 2024;23:102558. https://doi.org/10.1016/j.rineng.2024.102558
33. Yang H, Zhao M, Xing D, Zhang J, Fang T, Zhang F, et al. Contact lens as an emerging platform for ophthalmic drug delivery: A systematic review. Asian J Pharm Sci 2023;18:100847. https://doi.org/10.1016/J.AJPS.2023.100847

34. Shaker LM, Alamiery AA, Takriff M, Isahak WNRW. Nano-Titanium Oxide in Polymeric Contact Lenses: Short Communication. Nanomanufacturing 2022, Vol 2, Pages 71-81 2022;2:71–81. https://doi.org/10.3390/nanomanufacturing2030006
35. Docampo-Palacios ML, Ramirez GA, Tesfatsion TT, Okhovat A, Pittiglio M, Ray KP, et al. Saturated Cannabinoids: Update on Synthesis Strategies and Biological Studies of These Emerging Cannabinoid Analogs. Molecules 2023;28. https://doi.org/10.3390/molecules28176434
36. Mostovenko E, Canal CG, Cho MJ, Sharma K, Erdely A, Campen MJ, et al. Indirect Mediators of Systemic Health Outcomes Following Nanoparticle Inhalation Exposure. Pharmacol Ther 2022;235:108120. https://doi.org/10.1016/j.pharmthera.2022.108120
37. Dent, F. J., Harbottle, D., Warren, N. J., & Khodaparast, S. (2022). Temporally Arrested Breath Figure. ACS applied materials & interfaces, 14(23), 27435–27443. https://doi.org/10.1021/acsami.2c05635
38. Gao L, Zhang Q, Gu M. Femtosecond laser micro/nano processing: from fundamental to applications. International Journal of Extreme Manufacturing 2024;7:022010. https://doi.org/10.1088/2631-7990/ad943e
39. Wu S, Liu B, Su X, Zhang S. Structural Color Patterns on Paper Fabricated by Inkjet Printer and Their Application in Anticounterfeiting. Journal of Physical Chemistry Letters 2017;8:2835–41. https://doi.org/10.1021/acs.jpclett.7b01372
40. Shin CM, Cho S, Kim DH, Ha Y, Shin HJ, Shin N, et al. Zwitterionic polydopamine coatings suppress silicone implant-induced capsule formation. Biomater Sci 2021;9:3425–32. https://doi.org/10.1039/d0bm02215b
41. Wilson, C. J., Clegg, R. E., Leavesley, D. I., & Pearcy, M. J. (2005). Mediation of biomaterial-cell interactions by adsorbed proteins: a review. Tissue engineering, 11(1-2), 1–18. https://doi.org/10.1089/ten.2005.11.1
42. Sharmile N, Chowdhury RR, Desai S. A Comprehensive Review of Quality Control and Reliability Research in Micro–Nano Technology. Technologies 2025, Vol 13, Page 94 2025;13:94. https://doi.org/10.3390/technologies13030094
43. Huang Z, Cao L. Quantitative phase imaging based on holography: trends and new perspectives. Light Sci Appl 2024;13:145. https://doi.org/10.1038/s41377-024-01453-x
44. Bovone, G., Dudaryeva, O. Y., Marco-Dufort, B., & Tibbitt, M. W. (2021). Engineering Hydrogel Adhesion for Biomedical Applications via Chemical Design of the Junction. ACS biomaterials science & engineering, 7(9), 4048–4076. https://doi.org/10.1021/acsbiomaterials.0c01677
45. Gause S, Hsu KH, Shafor C, Dixon P, Powell KC, Chauhan A. Mechanistic modeling of ophthalmic drug delivery to the anterior chamber by eye drops and contact lenses. Adv Colloid Interface Sci 2016;233:139–54. https://doi.org/10.1016/j.cis.2015.08.002
46. He W, Wen J, Hu Q, Yi Y, Wei Z, Yang X, et al. The advances in zwitterionic materials and their biomedical applications. International Materials Reviews 2025. https://doi.org/10.1177/09506608251323568
47. Pucker AD, Tichenor AA. A Review of Contact Lens Dropout. Clin Optom (Auckl) 2020;12:85. https://doi.org/10.2147/opto.s198637
48. Liu L, Chen H, Zhao X, Han Q, Xu Y, Liu Y, et al. Advances in the application and research of biomaterials in promoting bone repair and regeneration through immune modulation. Mater Today Bio 2025;30:101410. https://doi.org/10.1016/j.mtbio.2024.101410
49. Hu, Y., Luo, Z., & Bao, Y. (2025). Trends in Photopolymerization 3D Printing for Advanced Drug Delivery Applications. Biomacromolecules, 26(1), 85–117. https://doi.org/10.1021/acs.biomac.4c01004

50. Duraccio D, Capra PP, Malucelli G. UV-curable coatings for energy harvesting applications: Current state-of-the-art and future perspectives. Micro and Nano Engineering 2024;23:100266. https://doi.org/10.1016/j.mne.2024.100266
51. Khanda M, Seal P, Mohan AJ, Arya N, Boda SK. Antimicrobial peptides and their application to combat implant-associated infections – opportunities and challenges. Nanoscale 2025;17:10462–84. https://doi.org/10.1039/d5nr00953g
52. Porcheri C, Meisel CT, Mitsiadis T. Multifactorial Contribution of Notch Signaling in Head and Neck Squamous Cell Carcinoma. Int J Mol Sci 2019;20:1520. https://doi.org/10.3390/ijms20061520
53. Muntz A, Subbaraman LN, Sorbara L, Jones L. Tear exchange and contact lenses: A review. J Optom 2015;8:2–11. https://doi.org/10.1016/j.optom.2014.12.001
54. Tsai HF, Podder S, Chen PY. Microsystem Advances through Integration with Artificial Intelligence. Micromachines 2023, Vol 14, Page 826 2023;14:826. https://doi.org/10.3390/mi14040826
55. Yang D, Han Y, Wang Y, Pan Y, Zheng L, Liu Z, et al. Highly effective corneal permeability of reactive oxygen species-responsive nano-formulation encapsulated cyclosporine a for dry eye management. Chemical Engineering Journal 2023;469:143968. https://doi.org/10.1016/j.cej.2023.143968